Seasonal Evolution of the Sea Ice Floe Size Distribution from Two Decades of MODIS Data

Ellen M. Buckley[1], Leela Cañuelas[1], Mary-Louise Timmermans[2], and Monica M. Wilhelmus[1]

[1]Center for Fluid Mechanics, School of Engineering, Brown University, Providence, RI, USA
[2]Department of Earth and Planetary Sciences, Yale University, New Haven, CT, USA

Correspondence: mmwilhelmus@brown.edu

Abstract. The Arctic sea ice cover seasonally evolves from large plates separated by long, linear leads in the winter to a mosaic of smaller sea ice floes in the summer. The interplay between physical and thermodynamic mechanisms during this process ultimately sets the observed sea ice floe size distribution (FSD), an important metric for characterizing the sea ice cover and assessing model performance. Historically, FSDs have been studied at fixed locations over short periods, leaving a gap in our understanding of the spatial and temporal evolution of the FSD at large scales. Here, we present a new framework for image segmentation, allowing the identification and labeling of individual ice floes in Moderate Resolution Imaging Spectroradiometer (MODIS) data. Using this algorithm, we automatically process and segment 4,861 images, identifying more than 9.4 million floes over 23 years. The extracted characteristics of the floes–including area, perimeter, and orientation–evolve throughout the spring and summer in the Beaufort Sea. We find seasonal patterns of decreasing mean floe area, increasing FSD power law slope, and more variability in the floe orientation as the summer progresses.

1 Introduction

The Arctic sea ice cover controls heat and moisture flux from the atmosphere to the ocean. It has an annual cycle characterized by the growth and melt of ice in which large, heterogeneous snow-covered winter ice floes fragment into an ensemble of smaller floes in the summer. The break-up of the ice cover and resulting floe size distribution (FSD) is set by complex feedback loops involving physical and thermodynamic processes. For instance, given the higher perimeter-to-area ratios of small floes compared to that of larger floes, small floes experience proportionally more lateral melting. This effect is observed to be especially pronounced for floes smaller than 50 m in diameter (Steele, 1992; Horvat et al., 2016). Lateral melting shrinks the floes, further raising their perimeter-to-area ratios, thus leading to a positive feedback cycle. Also, lateral melt creates density gradients that contribute to the non-homogeneous stratification of the upper ocean mixed-layer, enhancing mixing and eddy formation (Horvat et al., 2016). Long waves from summer Arctic storms fracture the ice pack (Asplin et al., 2012), an effect amplified by the retreating sea ice edge and lengthened open water fetch enhancing wave energy. The FSD also yields information about how a sea ice field will respond to oceanic and atmospheric forcing. Since the drag coefficient between an ice floe and the ocean depends on the ice floe size, FSD is related to ocean-atmosphere energy and momentum transfer (Birnbaum and Lüpkes, 2002).

25   Following the original conceptualization of floe size distribution in Rothrock and Thorndike (1984), numerous studies have documented floe size distribution in various regions throughout the Arctic and Antarctic (see Stern et al. (2018b) for a comprehensive list of FSD studies). We focus on the Beaufort Sea, where FSDs have previously been determined from radar imagery (Holt and Martin, 2001; Hwang et al., 2017), high resolution imagery (Wang et al., 2016; Denton and Timmermans, 2022), and aerial photography (Rothrock and Thorndike, 1984; Perovich and Jones, 2014). These studies have advanced our knowledge

30   of seasonal evolution of the FSD, the effect of storms on floe breakup, and the relationship between sea ice concentration and FSD. However, these studies are limited in both time and space, sampling small areas where observations are temporally sparse.

Moderate-resolution Imaging Spectroradiometer (MODIS) data have been previously used in floe size distribution studies (Toyota et al., 2016; Zhang et al., 2016; Stern et al., 2018a), but only for short term studies over a few years at most. (Lopez-

35   Acosta et al., 2019) demonstrate the ability to segment MODIS image, identify ice floes, and track individual floes over consecutive images. The Ice Floe Tracker (IFT) algorithm (Lopez-Acosta et al., 2019) has previously been used to identify eddies in the Beaufort Sea (Manucharyan et al., 2022), to initialize and validate floe shapes in models (Chen et al., 2022), and to understand the factors affecting sea ice motion in the Greenland Sea (Watkins et al., 2023). The IFT algorithm was designed to accurately track individual pieces of sea ice over time, requiring the same floes to appear in consecutive images. In this

40   work, we focus on maximizing the number of identified floes in a range of sea ice conditions to better capture the floe size distribution. We develop a new algorithm based on (Denton and Timmermans, 2022) that focuses on high identification rates of ice floes and retrieving accurate geometric properties. Although the visible imagery is limited to time periods with available sunlight, this 23-year dataset provides the potential to massively expand our floe database and FSD studies. First we present an algorithm for image segmentation and floe identification in images of ice in a range of ice concentration and melt states.

45   We validate the extracted sea ice floe properties with higher resolution data and existing datasets. Then, the floe identification algorithm is applied to thousands of MODIS images spanning from 2000-2022, from March through September in the Beaufort Sea. The seasonal evolution and interannual variability of the floe sizes are presented and discussed. We conclude the study with an overview of our findings and suggestions for future directions.

2   Study Area and Data

50   The Beaufort Sea has experienced profound changes over recent decades. The end of summer sea ice area, measured as the September monthly average, is decreasing at a rate of 10-30% per decade (Timmermans and Toole, 2023), resulting in substantially more solar heating in the upper ocean. The older and thicker multiyear ice is now melting out during summer within the Beaufort Sea (Kwok and Cunningham, 2010) and the multiyear ice edge is receding (Galley et al., 2016). We focus on this region in our study (Fig. 1a) because it is important to understand this rapidly changing region and we expect to see a

55   marked transition seasonally from high concentration winter sea ice to the melting fractured sea ice of summer.
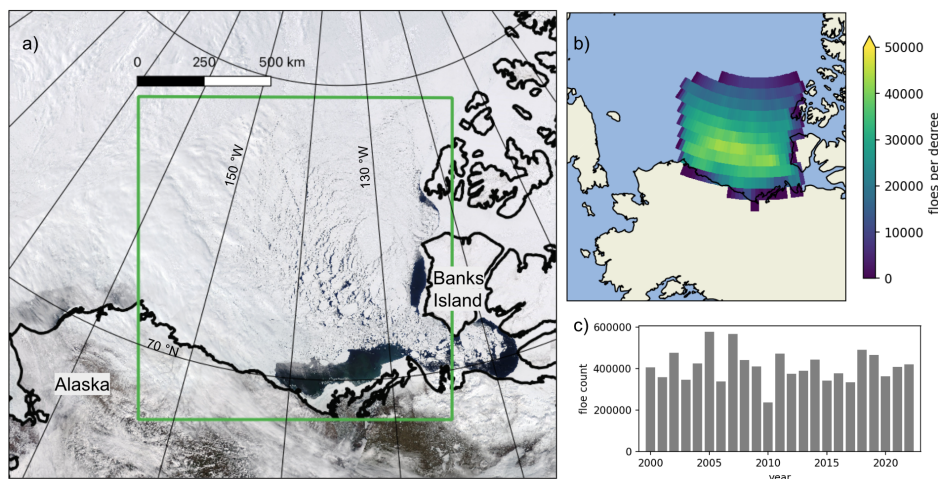
Figure 1. Study region. a) True Color MODIS imagery of the Beaufort Sea on 22 May 2021, the study region is outlined in a green box. b) location density of observed floes in the study region. c) distribution of observed floes by year.

2.1 MODIS Imagery

The Moderate Resolution Imaging Spectroradiometer (MODIS) instrument is onboard two NASA satellites, Terra and Aqua, launched in 1999 and 2002, respectively. MODIS acquires data in 36 spectral bands spanning wavelengths from 0.4 to 14.4 μm with varying resolution. In this work we use the True Color imagery (Fig. 1a), a composite of Band 1 (red, 645 nm),
60 Band 4 (green, 555 nm), and Band 3 (blue, 469 nm) (Vermote, 2015). This composite product is available at 250 m resolution. The MODIS Cloud Product (MOD06/MYD06, (Platnick et al., 2016)) reports calculated cloud properties for each pixel in the MODIS images and includes a cloud fraction derived from the infrared imagery. We use the cloud fraction parameter to mask out the cloudy regions in the pre-processing step of the algorithm (Section 3.1). The acquired imagery, both true color and cloud fraction data, spans the extent of the green box in Figure 1a.

65 ## 2.2 Sentinel-2 Imagery

The Sentinel-2 satellites A and B, launched in 2015 and 2017, carry the multispectral instrument, acquiring data in 13 spectral bands. Sentinel-2 imagery is available up to 20 km off the coast. Four bands provide data at 10 m resolution: Band 2 (blue, 492.3 nm), Band 3 (green, 558.9 nm), Band 4 (red, 664.9 nm), and Band 8 (near infrared, 832.9 nm) (Drusch et al., 2012). In this work we use the high-resolution Sentinel-2 data to understand the limitations of the moderate resolution MODIS imagery.

70 ## 3 Image Segmentation Methodology

The algorithm described here builds on the segmentation and identification routine in (Denton and Timmermans, 2022), which uses the erosion-expansion techniques described in (Paget et al., 2001). We rewrite the algorithm in python, and automate it
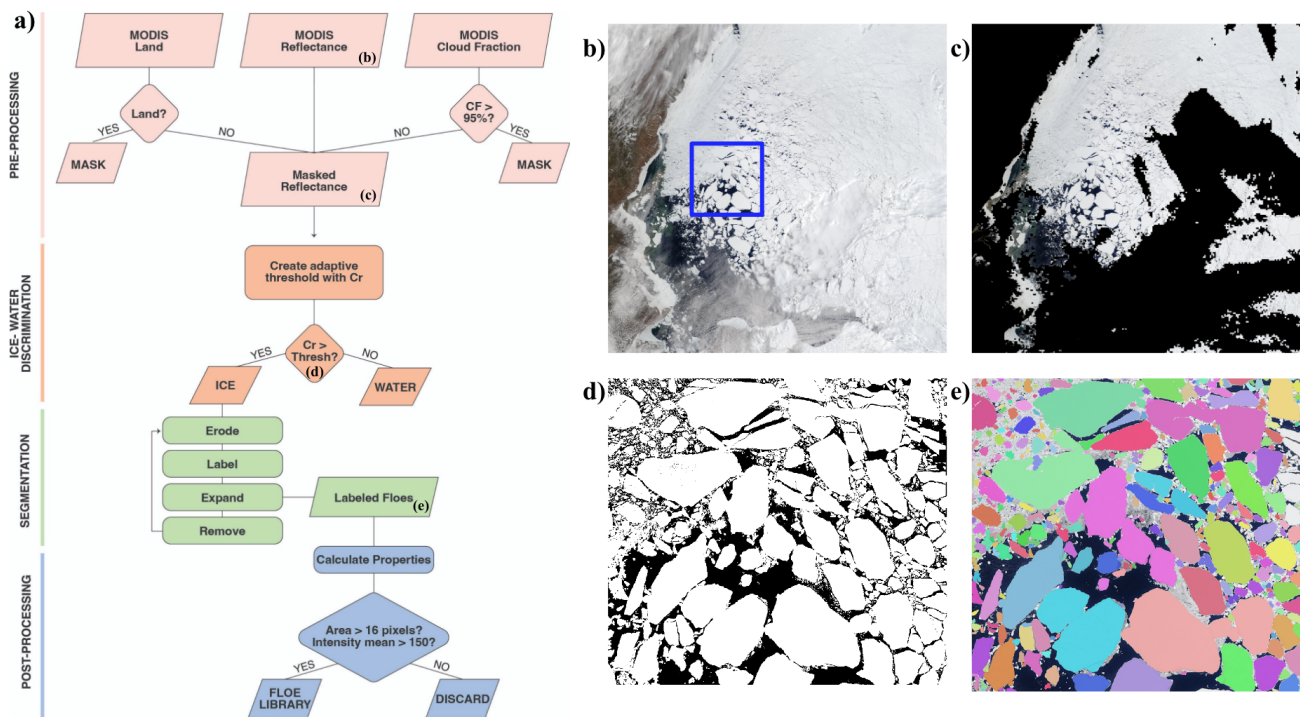
Figure 2. Image segmentation methodology. a) flow diagram showing the steps of the algorithm: pre-processing (pink), ice-water discrimination (orange), segmentation (green), and post-processing (blue). b) the original MODIS true color reflectance imagery in the region of interest. The blue square shows the location of d) and e). c) the MODIS true reflectance data with a mask (black) over the land and cloudy regions. d) ice water discrimination results showing ice (white) and water or mask (black). e) final segmented image showing individual floes in different colors. The example MODIS image shown here is from 10 June 2017.

to process thousands of images consecutively, and introduce adaptive thresholds. The algorithm consists of four steps: pre-processing, ice-water discrimination, segmentation, and post-processing (Figure 2).

3.1 Pre-Processing

We use the MODIS True Color Reflectance data as a starting point for our analysis and to ensure we process only clear-sky, ocean imagery, we mask the land and the cloud-covered areas. Because any amount of cloud cover can blur the edges of the floes, we are conservative with cloud cover and use the existing MODIS cloud fraction data to eliminate areas that may be affected by clouds. We mask the areas with $\geq 95\%$ cloud coverage according to the MODIS cloud fraction product (Section 2.1, Fig. 2c). The presence of clouds in the Arctic in the summer is ubiquitous; on average 71% of an image is covered in clouds (Figure 5d).

3.2 Ice-Water Discrimination

The images cover a large area with a range of ice conditions, i.e. from the ice edge into the pack ice region, and we cannot apply a simple threshold pixel value to distinguish the bright ice from the dark open water pixels (as in (Denton and Timmermans, 2022)). The thin leads that separate the large floes in the spring may be covered by a thin layer of ice increasing the brightness of the lead beyond the typical brightness values of the open ocean. Similarly, the ubiquitous low-lying fog in the summer Arctic may locally brighten the appearance of open water. To combat the variable pixel values of open water, we apply an adaptive threshold to determine local values for the ice-water discrimination. We apply this method to the red channel band of the MODIS imagery which exhibits the highest contrast in pixel values. The dynamic threshold value is the weighted mean for the 400-pixel (100 km) neighborhood of a pixel subtracted by a constant. All pixels with brightness greater (less) than the threshold are identified as ice (open water).

3.3 Image Segmentation

The image segmentation step follows an erosion-expansion routine similar to that described in Paget et al. (2001) and subsequent studies segmenting airborne and satellite imagery of sea ice floes (e.g., Denton and Timmermans, 2022; Steer et al., 2008). The input to the segmentation routine is the binary classified image created in the previous step (section 3.2), where where 1 represents the sea ice and 0 is the open water. The morphological erosion operation is applied to the binary image, removing pixels on the object boundaries. The binary image is eroded a total of eight times in order to ensure that floes are separated. The eight iteration removes small floes from the image. At this point, the remaining distinct objects are tagged, and then regrown (dilated) to their original state. The regrown tagged floes are then removed from the binary image, i,e, changed from 1 to 0. This erosion-tag-expansion is repeated, with fewer erosions each time, allowing for subsequently smaller floes to be identified with each iteration. In this way, sea ice floes of varying sizes are separated and identified. At the end of the image segmentation routine, an image with each unique object labelled is produced. However, some areas of sea ice, such as those consisting of ice filaments, brash ice or very small pieces of ice, are not able to be identified as individual floes. On average, 26% of the classified sea ice area is identified as individual floes. After processing years 2000-2022, from day-of-year 60-274 (approximately March 1- September 30, encompassing the time of year when light levels are sufficiently high for optical imagery), we segmented 4861 images (days), identifying 9,448,563 floes.

3.4 Post-Processing

The following geometrical parameters are calculated for each identified floes: area, perimeter, major and minor axis, centroid position, orientation, and intensity mean. The intensity mean is the average red channel value for the extent of the floe. The orientation of a floe is defined as the angle of the major axis of the floe from polar stereographic North. Orientation values from from $-\frac{\pi}{2}$ to $\frac{\pi}{2}$. The circular standard deviation of the orientation is calculated to represent the variation of the floe orientation, with low standard deviation representing floes aligned in the same direction, and high standard deviation in images with no

preferred directional alignment of floes. We also calculate the circularity of a floe:

$$C = \frac{4\pi A}{P^2} \tag{1}$$

where A is the floe area, P is the floe perimeter, and circularity of a circle, the maximum circularity, is C = 1.

We take several steps to ensure each identified object is a floe. We examine the intensity mean of the floes, and discard floes with a mean red channel pixel intensity less than 150, an empirically determined value. Image pixels on ice floes have high red channel values, and thus objects with a low intensity mean may be incorrectly identified objects, such as clusters of brash ice. This quality assurance steps result in an elimination of 86,501 floes (<1% of total floes).

3.5 Floe Size Distribution

The floe size distribution (FSD) contributes to the characterization of the ice floe field by providing a quantitative description of the ice floe area statistics that complements other parameters commonly used to describe floe fields, such as the sea ice concentration (SIC) and average ice thickness. Together, these measures provide a set of tools with which we can directly characterize the geometry of the Arctic ice pack (Section 3.4) and so indirectly study the physical processes that shape this geometry. We utilize the powerlaw Python package (Alstott et al., 2014) based on the maximum likelihood estimation power law fitting methods described in Clauset et al. (2009) and Klaus et al. (2011). The non-cumulative power law is described by:

$$p(x) = cx^{-\alpha} \tag{2}$$

where $p(x)$ is the probability of a given instance of x, the chosen geometric property of the sea ice floe (we use floe area), c is a normalization constant ensuring that the function integrates to 1, and α is the fitted parameter and slope of the power law distribution. Here, we use α and power law slope interchangeably. The standard error of the fitted distribution is defined in Clauset et al. (2009) as:

$$\sigma = \frac{\alpha - 1}{\sqrt{n}} + O(1/n) \tag{3}$$

where n is the sample size, and the higher order correction is positive. We calculate the floe size distribution power law fit for different data sets to understand how the ice cover evolves, seasonally and annually.

3.6 Validation and Limitations

We evaluate the consistency of the algorithm by examining the floes extracted from Aqua and Terra images on the same day. We expect a very similar power law distribution of identified floe sizes on the same day from the two different satellites that carry the same MODIS instrument. We randomly selected 100 days to examine both Aqua and Terra images. We segment both images, calculate floe properties, and match floes based on centroid location. We find a correlation value of 0.99 for the matched floes areas. For each pair of images where each image has at least 50,000 km^2 of identified floes, we fit a power law to the floe area distribution (Section 3.5), and determine the slope (α). We find an absolute mean difference in the Aqua and

Terra α values of 0.009 and a standard deviation of 0.006. This suggests a strong agreement between the floes identified in the Aqua and Terra satellite imagery, confirming that the IFT is consistently identifying floes.

145 To understand and quantify the limitations of the moderate-resolution imagery used by the IFT, we apply the IFT to higher resolution 10-m Sentinel-2 imagery. We examine spatially coincident MODIS imagery and Sentinel-2 imagery observed on the same day (Fig. 3). The extents of the two images are matched, so that the same area is analyzed. We evaluate imagery in a range of sea ice conditions: low SIC (40%) seen at the end of the summer (Fig. 3a-c), ice in the marginal ice zone in summer (70% SIC, Fig. 3d-f), and high SIC (98%) at the beginning of the melt season (Fig. 3g-i). We pair floes identified in the coincident imagery based on centroid location and examine the corresponding floe properties. The areas of the matching

150 82 floes agree very well, with a correlation of 0.99, and an absolute mean area difference of 0.18 km^2 (Figure 4). A power law is fit to the floe size distribution for each of the images with the minimum floe area set to to minimum observable floe size in the MODIS imagery, xmin = 5 km^2. Approximately 82% of the floes identified in the Sentinel-2 imagery are less than the determined xmin value for the MODIS imagery. However in the overlapping range of floe areas (x$\geq$5), 14% more floes are identified in the MODIS imagery compared to the Sentinel-2 imagery. The higher resolution allows for identification of smaller

155 floes but performs similarly to the lower resolution imagery when it comes to larger floes. Thus, the image segmentations yield similar floe size distribution α values. The difference in α values range from 0.03 to 0.21, with 1-sigma confidence intervals overlapping for the low and high SIC instances (Fig. 3c and i), and 2-sigma overlap for the medium SIC example (Fig. 3f). Despite the limitations of the resolution of smaller floes in the MODIS imagery, our validation shows that the algorithm applied to the MODIS imagery samples the floe sizes sufficiently to produce an accurate FSD α value, and that the floes identified in

160 both images have highly correlated floe areas.

Finally, we apply a bootstrap approach to quantify uncertainty in the derived parameters. We randomly select 100 days of segmented images ensuring each of these day has at least 50,000 km^2 of identified floes, and for each of those days examine the uncertainty in the derived floe size distribution. We create 1000 bootstrap samples with replacement. Each bootstrapped sample is the length of the original dataset (the number of identified floes in the image), and we calculate the power law distribution

165 of the sampled floe areas. We then calculate the standard deviation of the α values for each image. The standard deviation of α generated from the bootstrapping of an image is on average, 0.024, ranging from 0.007 to 0.08. The the standard deviation increases as the α values increases, indicating more uncertainty.

We chose to analyze MODIS imagery due to its long record and consistent coverage, but other higher resolution imagery is required to examine the floe size distribution for floes smaller than 5 km^2. Other studies have examined FSD in SAR imagery

170 which eliminates the need for clear-sky conditions as SAR is not sensitive to clouds. However, SAR data is not as widely available, and has a other limitations and complications, such as speckle, or granular noise.
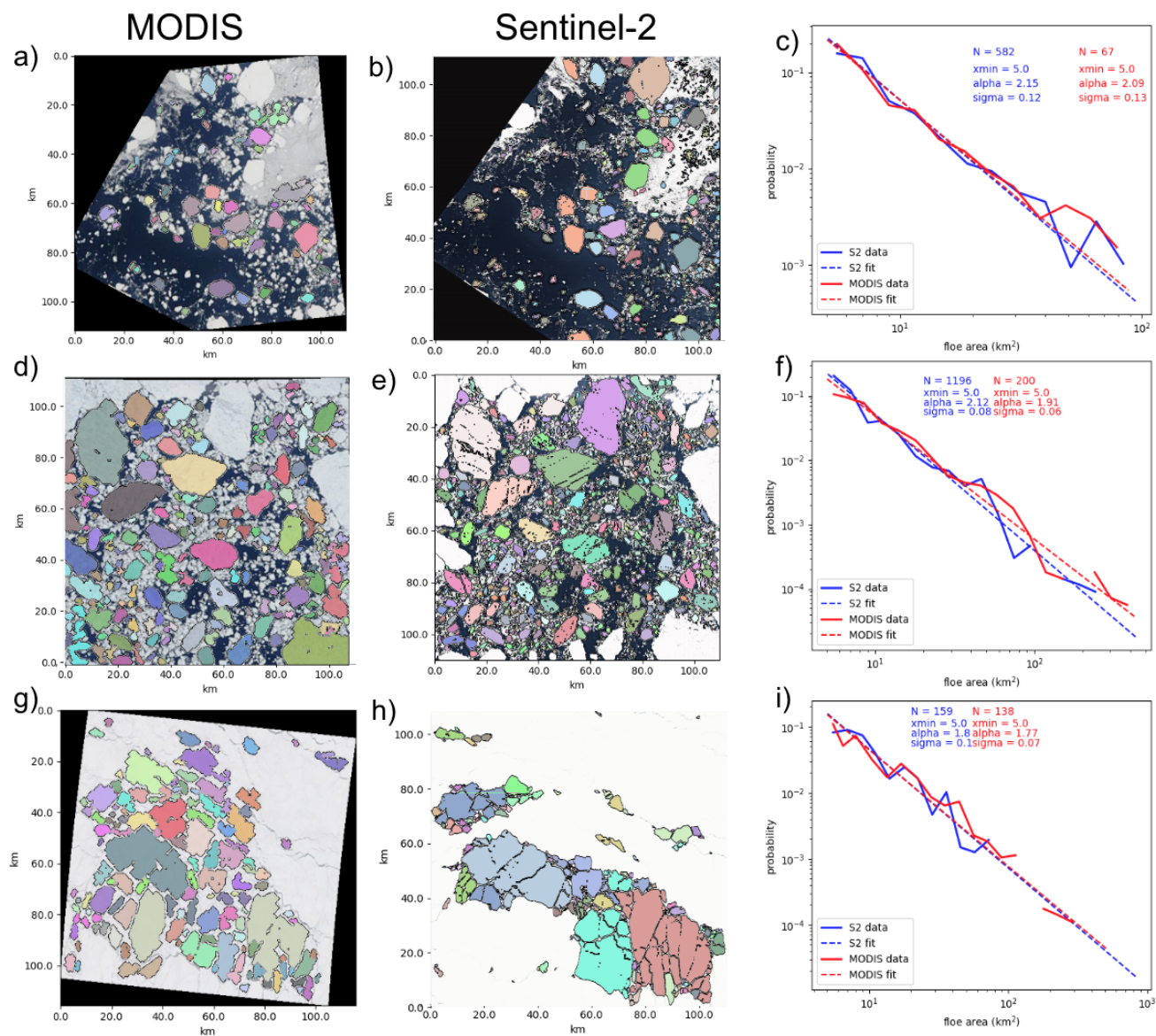
Figure 3. Validation of MODIS imagery segmentation with higher-resolution (10m) Sentinel-2 imagery. Each row shows spatially coincident MODIS (first column) and Sentinel-2 (second column) imagery captured on the same day. The segmentation algorithm is applied to each of these images and the individual identified floes are colored in the imaeg. The third column shows the PDF of the floe size distribution for Sentinel-2 (blue) and MODIS (red) images, with the best fit power law shown as the dashed line. The three rows are for imagery capture on 4 September, 2019, 12 June, 2020, and 14 May, 2021.
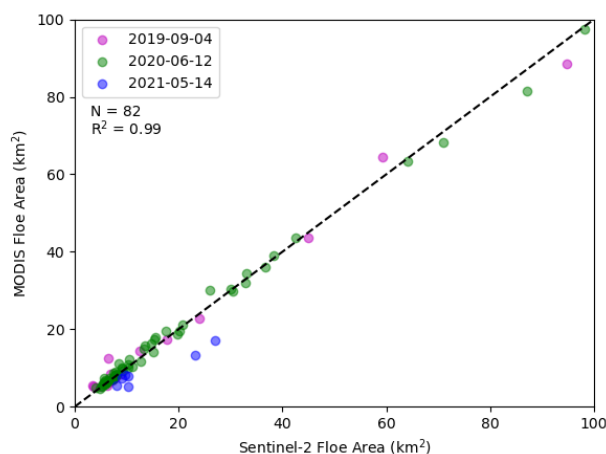
Figure 4. Area comparison of the 82 floes identified in both MODIS and Sentinel-2 imagery (Fig. 3) with the dot color corresponding to the date of the image: 2019-09-04 (pink), 2020-08-22 (green), and 2021-05-14 (blue).

4 Spring to Summer Transition of Floe Characteristics

4.1 Floe Area

In the spring, the Beaufort Sea ice cover has high ice concentration consisting of large floes with rectilinear fractures. During the summer, as the ice edge recedes from the Alaskan and Canadian shorelines, the ice cover transitions to a dynamic collection of randomly oriented floes among brash ice. We monitor floe characteristics from March 1 through September 30 in the MODIS imagery and observe patterns corresponding to this transition. The mean floe area first increases from 75 km^2 on 6 March to the seasonal high of 103 km^2 on 10 April (Fig. 5a, blue). Mean floe area then decreases throughout the summer, plateauing in August around 24 km^2 and then increases to reach a mean area of 30 km^2 by the end of September. The median floe area is consistently lower than the mean floe area (Fig. 5a, orange), as the distribution is positively skewed with many small floes. The median floe size exhibits a similar pattern as the mean, with a maximum median value of 17 km^2 on 10 April, decreasing to 12 km^2 30 September. We also see the largest floes existing in the areas of highest sea ice concentration (Fig. 7b), ice conditions that exist in the early spring. Floes that exist in areas of low ice concentration are more likely to experience the effect of waves, and may break up into smaller floes due to wave fracture (Squire et al., 1995).

4.2 Power Law Fit to Floe Size Distribution

We fit a power law to the collection of floes in the running 10-day window. The value of α (slope of the power law distribution) of all floes identified is 1.85, but ranges from 1.74 to 2.0 throughout the summer (Fig. 5b). The standard deviations and the confidence intervals of all power law fits is < 0.01. The power law α is inversely correlated to the mean floe area; the
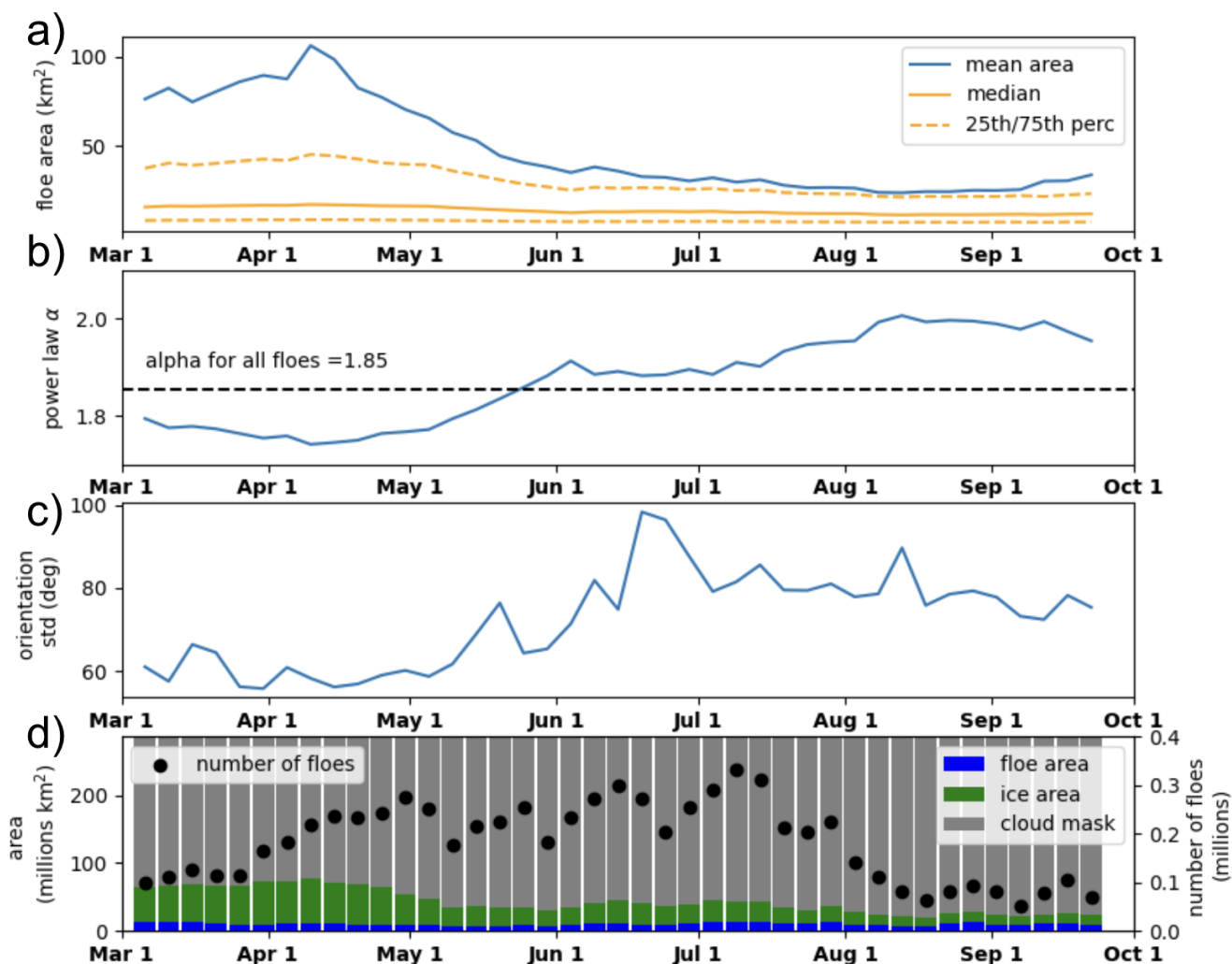
Figure 5. Spring through summer evolution of floe properties. The properties were aggregated into a 10-day running window and sampled every 5 days. a) mean (blue), median (orange, solid) and 25th/75th percentiles (orange, dashed) of floe area. b) the slope anomaly about the power law slope fitted to all floes in the dataset. Negative (positive) indicate a power law slope flatter (steeper) than the slope of the power law fit to all floes (1.85). c) standard deviation of the orientation of floes for all floes (blue), and for large, low circularity floes (green, area > 75th percentile, 29 km^2, circularity < 25th percentile, 0.5). d) total areas and number of floes analyzed for the 5-day statistics presented in a)-c). The total analyzed area (blue) is the total area that is not masked by land (magenta) or clouds (gray), ice area (green) is the ice identified within the unmasked area, and the black dots show the total number of floes.

slope value decreases from the beginning of March to the minimum in mid April, then increases throughout the summer to

190 a maximum on 18 August, and slowly begins to decrease again for the remainder of the summer. The inverse relationship to mean floe area is expected, as a higher frequency of small floes will decrease the mean floe area and increase the slope of the floe size distribution fit. The floe size distribution trend is consistent with previous studies that have taken a Lagrangian approach, tracking the same ice throughout the summer. During the Surface Heat Budget of the Arctic (SHEBA) campaign in 1998 in the Beaufort and Chukchi Seas aerial photography was collected in the proximity of the ship. (Perovich and Jones,

195 2014) found floe size distribution power law slope values increased through the summer, reached a maximum on 10 August, and subsequently decreased into September as small floes froze and fused into larger floes (Perovich and Jones, 2014). (Hwang et al., 2017) observed FSD in satellite Synthetic Aperture Radar (SAR) imagery tracking four buoys in the Beaufort Sea in 2014 and capturing images of the same ice, finding an increase in FSD α values from July through August with enhanced floe breakup linked to wind events.

200 We examine the FSD power law slope over the 23-year record to quantify the interannual variability and discern any decadal trends. As the FSD exhibits seasonal variability we look at the monthly FSD power law slopes and compare over the years. We see no significant trends in the monthly FSD slopes over the 23-year (Fig. 6). The error on all calculated alpha values is < 0.01 as determined by 1000 bootstrap samples to calculate a 95% confidence interval, and the standard deviation calculated as in Equation 3. The month of September exhibits the most variability with α values ranging from 1.85 to 2.17 (Fig. 5b,shaded,

205 and 6). One may expect a trend towards larger α values (steeper FSD power law slopes) as the Beaufort Sea ice cover exhibits earlier retreat (Fetterer et al., 2017) and a transition to first year ice that is more susceptible to fracture (Galley et al., 2016), however this is not exhibited in our data. This lack of a significant decadal trend in FSD slope may be due to the large study region that simultaneously contains pack ice and open water, or, because MODIS cannot resolve floes smaller than 5 km^2 in area, there may be many more small floes in recent years that are not identified in the MODIS data.

210 A similar study conducted by Stern et al. (2018a) examining 116 MODIS images in 2013 and 2014 fit a power law to floes ranging from 2 to 30 km in size, which is aproximately equivalent to 2.64 to 59400 km^2 (Rothrock and Thorndike, 1984). They found the same pattern of the FSD slope, but larger values. In May they found α= 2.0, increasing to 2.9 in July, and then decreasing back to 2.2 by October. Although we observe a similar evolution of the alpha value, our power law slope is much shallower. This could be due to the segmentation methodology and the location of the observed floes. Our algorithm was

215 applied widely to all clear areas of MODIS imagery, meaning that we could be observing more large floes within the ice pack. Also, an error arise when the algorithm is not able to separate floes, particularly when they are only separate by small cracks, thus potentially biasing the floe sizes larger. Our wider application of the image segmentation could mean our alpha values are biased low compared to other studies with smaller sample sizes and the ability to manually validate the image segmentation.

4.3 Floe Orientation

220 In the late winter and spring, the Beaufort has high sea ice concentration. As external stresses, such as wind stress, are applied to the ice pack, the ice pack experiences strain, leading to fracture in a preferential direction that depend on the force's orientation relative to the coast (Lewis and Hutchings, 2019; Jewell et al., 2023). When we examine the newly fractured floes during
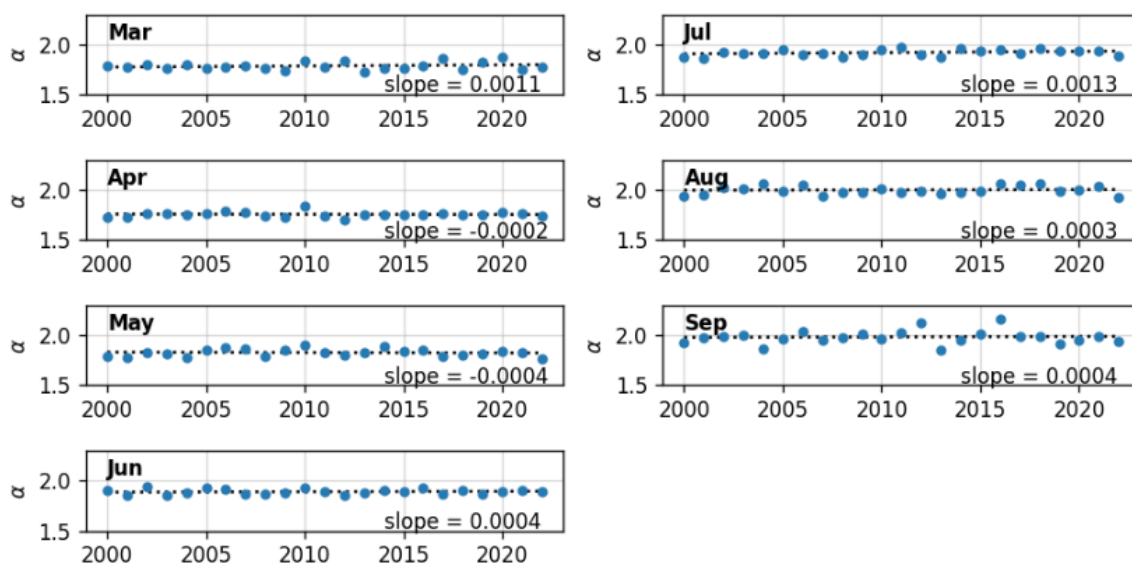
Figure 6. α values of a power law fitted floe size distribution for each month of analysis. Each strip shows the α value for all floes identified in that month over the 23-year analysis. The dotted line is the line of best fit, the slope of which is printed in the bottom right hand corner of each strip.

this time period, we find a low variability in their orientation (Fig. 5c). This effect is especially noticeable in areas of high ice concentration, where the ice movement and readjustment to external forces is limited by the surrounding ice (Fig. 7a). The small

225 fractures, or cracks, grow into leads that are can be seen in the MODIS imagery (e.g., Fig. 3g). As the summer progresses, SIC decreases and ice floes break up and disperse, resulting in a decreasing average floe area (Fig. 5a) and no preferential direction for floe orientation (Figs. 5c and 7). We also examine the large rectilinear floes that we expect are most likely to exhibit this pattern of orientation. We limit the sample to large floes ($>$75th percentile, 29 km^2) and low circularity floes ($<$25th percentile, 0.5, or approximately the circularity of a 1:4 rectangle), in total, about 17% of the data. This subset displays a lower orientation

230 variability in the beginning of the season as compared to the full data set, but increasing in variability into the summer as in the full data set.

5   Conclusions

In this study we segment and identify individual sea ice floes in MODIS imagery and find a seasonally evolving floe size distribution. The identified floes are validated visually and with higher-resolution Sentinel-2 imagery, demonstrating that in the

235 specified range of floes with area greater than 5 km^2, the segmentation algorithm performs equally well on images of moderate
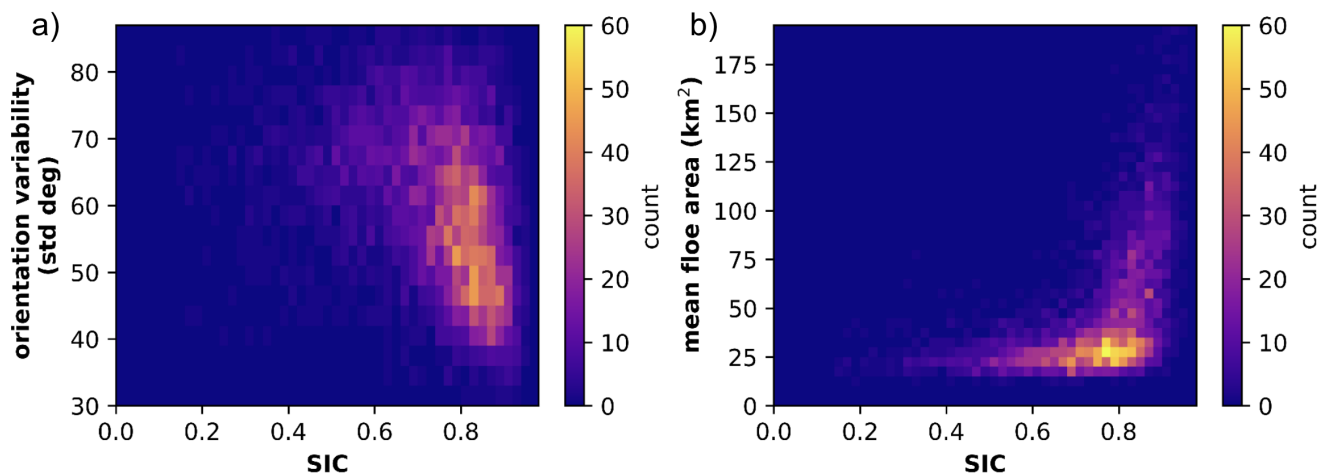
Figure 7. Observed floe properties compared to ice concentration (SIC). a) standard deviation of the orientation of floes in an image compared to the image SIC. b) mean floe area in an image compared to the image SIC. The colorbar indicates total image count.

resolution (MODIS) and high resolution (Sentinel-2). This allows us to confidently apply this systematic method to analyze thousands of images over 23 years covering a wide range of ice conditions.

We examine the seasonal evolution of floe size distribution and aspects of the floe geometry in the Beaufort Sea. We find from mid-April through early August, a decrease in the mean and median floe size, increasing power law slopes, and an increase in the variability in the orientation of the floes. As the sea ice cover appears and behaves drastically differently depending on the time of year, it is essential to use floe characteristics from the specific time period of interest when evaluating or tuning discrete element models.

The algorithm developed in this study establishes the ability to derive meaningful information on floe sizes from moderate resolution images. This MODIS imagery has Arctic wide coverage and spans 23 years. This expansive dataset combined with the new segmentation algorithm presented here allows for continued study of ice conditions and characteristics in the spring and summer. Future work may show regional differences in floe characteristics and timing of floe break up in the summer. Combining this new information with existing satellite measurements (e.g., ice drift, ice type, ice thickness) can provide further insights into the behavior of the ice pack. While no significant decadal trends were observed in the monthly floe size distribution over the 23-year period, future work considering smaller spatial domains may be necessary to investigate interannual and decadal variability in detail.

We chose to analyze MODIS imagery due to its long record and consistent coverage, but other higher resolution imagery is required to analyze the floe size distribution

Further work will include incorporating this image segmentation algorithm into the pipeline of the Ice Floe Tracker algorithm (Lopez-Acosta et al., 2019). This routine tracks floes with similar characteristics between consecutive MODIS images and can thus determine ice velocities and rotation rates, inferring ocean dynamics in regions that are otherwise under-observed. With

13

a new segmentation algorithm, able to identify floes in a wider range of sizes, we can uncover more information about the underlying ocean.

Code and data availability. Code will be made available upon acceptance of manuscript to a public Github repository. Data will be made available upon acceptance of manuscript on Zenodo

260 *Author contributions.*

MMW conceived of the study. EB wrote the algorithm and applied it to the imagery. MLT and LC supported the analysis of the results. All authors contributed to the writing of the paper.

Competing interests. We declare that no competing interests are present.

References

Alstott, J., Bullmore, E., and Plenz, D.: powerlaw: a Python package for analysis of heavy-tailed distributions, PloS one, 9, e85 777, 2014.

Asplin, M. G., Galley, R., Barber, D. G., and Prinsenberg, S.: Fracture of summer perennial sea ice by ocean swell as a result of Arctic storms, Journal of Geophysical Research: Oceans, 117, 2012.

Birnbaum, G. and Lüpkes, C.: A new parameterization of surface drag in the marginal sea ice zone, Tellus A: Dynamic Meteorology and Oceanography, 54, 107–123, 2002.

Chen, N., Fu, S., and Manucharyan, G. E.: An efficient and statistically accurate Lagrangian data assimilation algorithm with applications to discrete element sea ice models, Journal of Computational Physics, 455, 111 000, 2022.

Clauset, A., Shalizi, C. R., and Newman, M. E.: Power-law distributions in empirical data, SIAM review, 51, 661–703, 2009.

Denton, A. A. and Timmermans, M.-L.: Characterizing the sea-ice floe size distribution in the Canada Basin from high-resolution optical satellite imagery, The Cryosphere, 16, 1563–1578, 2022.

Drusch, M., Del Bello, U., Carlier, S., Colin, O., Fernandez, V., Gascon, F., Hoersch, B., Isola, C., Laberinti, P., Martimort, P., et al.: Sentinel-2: ESA's optical high-resolution mission for GMES operational services, Remote sensing of Environment, 120, 25–36, 2012.

Fetterer, F., Knowles, K., Meier, W. N., Savoie, M., and Windnagel, A. K.: Sea Ice Index, Version 3, https://doi.org/10.7265/N5K072F8, 2017.

Galley, R. J., Babb, D., Ogi, M., Else, B., Geilfus, N.-X., Crabeck, O., Barber, D. G., and Rysgaard, S.: Replacement of multiyear sea ice and changes in the open water season duration in the B eaufort S ea since 2004, Journal of Geophysical Research: Oceans, 121, 1806–1823, 2016.

Holt, B. and Martin, S.: The effect of a storm on the 1992 summer sea ice cover of the Beaufort, Chukchi, and East Siberian Seas, Journal of Geophysical Research: Oceans, 106, 1017–1032, 2001.

Horvat, C., Tziperman, E., and Campin, J.-M.: Interaction of sea ice floe size, ocean eddies, and sea ice melting, Geophysical Research Letters, 43, 8083–8090, 2016.

Hwang, B., Wilkinson, J., Maksym, T., Graber, H. C., Schweiger, A., Horvat, C., Perovich, D. K., Arntsen, A. E., Stanton, T. P., Ren, J., et al.: Winter-to-summer transition of Arctic sea ice breakup and floe size distribution in the Beaufort Sea, Elem Sci Anth, 5, 40, 2017.

Jewell, M. E., Hutchings, J. K., and Geiger, C. A.: Atmospheric highs drive asymmetric sea ice drift during lead opening from Point Barrow, The Cryosphere, 17, 3229–3250, https://doi.org/10.5194/tc-17-3229-2023, 2023.

Klaus, A., Yu, S., and Plenz, D.: Statistical analyses support power law distributions found in neuronal avalanches, PloS one, 6, e19 779, 2011.

Kwok, R. and Cunningham, G.: Contribution of melt in the Beaufort Sea to the decline in Arctic multiyear sea ice coverage: 1993–2009, Geophysical Research Letters, 37, 2010.

Lewis, B. J. and Hutchings, J. K.: Leads and associated sea ice drift in the Beaufort Sea in winter, Journal of Geophysical Research: Oceans, 124, 3411–3427, 2019.

Lopez-Acosta, R., Schodlok, M., and Wilhelmus, M.: Ice Floe Tracker: An algorithm to automatically retrieve Lagrangian trajectories via feature matching from moderate-resolution visual imagery, Remote Sensing of Environment, 234, 111 406, 2019.

Manucharyan, G. E., Lopez-Acosta, R., and Wilhelmus, M. M.: Spinning ice floes reveal intensification of mesoscale eddies in the western Arctic Ocean, Scientific Reports, 12, 7070, 2022.

https://doi.org/10.5194/egusphere-2024-89
Preprint. Discussion started: 19 January 2024
© Author(s) 2024. CC BY 4.0 License.

Paget, M., Worby, A., and Michael, K.: Determining the floe-size distribution of East Antarctic sea ice from digital aerial photographs, Annals of Glaciology, 33, 94–100, 2001.

305 Perovich, D. K. and Jones, K. F.: The seasonal evolution of sea ice floe size distribution, Journal of Geophysical Research: Oceans, 119, 8767–8777, 2014.

Platnick, S., Meyer, K. G., King, M. D., Wind, G., Amarasinghe, N., Marchant, B., Arnold, G. T., Zhang, Z., Hubanks, P. A., Holz, R. E., et al.: The MODIS cloud optical and microphysical products: Collection 6 updates and examples from Terra and Aqua, IEEE Transactions on Geoscience and Remote Sensing, 55, 502–525, 2016.

310 Rothrock, D. A. and Thorndike, A. S.: Measuring the sea ice floe size distribution, Journal of Geophysical Research: Oceans, 89, 6477–6486, 1984.

Squire, V. A., Dugan, J. P., Wadhams, P., Rottier, P. J., and Liu, A. K.: Of ocean waves and sea ice, Annual Review of Fluid Mechanics, 27, 115–168, 1995.

Steele, M.: Sea ice melting and floe geometry in a simple ice-ocean model, Journal of Geophysical Research: Oceans, 97, 17 729–17 738,
315   1992.

Steer, A., Worby, A., and Heil, P.: Observed changes in sea-ice floe size distribution during early summer in the western Weddell Sea, Deep Sea Research Part II: Topical Studies in Oceanography, 55, 933–942, 2008.

Stern, H. L., Schweiger, A. J., Stark, M., Zhang, J., Steele, M., and Hwang, B.: Seasonal evolution of the sea-ice floe size distribution in the Beaufort and Chukchi seas, Elementa: Science of the Anthropocene, 6, 2018a.

320 Stern, H. L., Schweiger, A. J., Zhang, J., and Steele, M.: On reconciling disparate studies of the sea-ice floe size distribution, Elem Sci Anth, 6, 49, 2018b.

Timmermans, M.-L. and Toole, J. M.: The Arctic Ocean's Beaufort Gyre, Annual Review of Marine Science, 15, 223–248, 2023.

Toyota, T., Kohout, A., and Fraser, A. D.: Formation processes of sea ice floe size distribution in the interior pack and its relationship to the marginal ice zone off East Antarctica, Deep Sea Research Part II: Topical Studies in Oceanography, 131, 28–40, 2016.

325 Vermote, E.: MOD09A1 MODIS Surface Reflectance 8-Day L3 Global 500 m SIN Grid V006, NASA EOSDIS Land Processes DAAC, USGS Report, 2015.

Wang, Y., Holt, B., Erick Rogers, W., Thomson, J., and Shen, H. H.: Wind and wave influences on sea ice floe size and leads in the B eaufort and C hukchi S eas during the summer-fall transition 2014, Journal of Geophysical Research: Oceans, 121, 1502–1525, 2016.

Watkins, D. M., Bliss, A. C., Hutchings, J. K., and Wilhelmus, M. M.: Evidence of abrupt transitions between sea ice dynamical regimes in
330   the East Greenland marginal ice zone, Geophysical Research Letters, 50, e2023GL103 558, 2023.

Zhang, J., Stern, H., Hwang, B., Schweiger, A., Steele, M., Stark, M., and Graber, H. C.: Modeling the seasonal evolution of the Arctic sea ice floe size distributionArctic sea ice floe size distribution, Elementa: Science of the Anthropocene, 4, 2016.